

Three dimensional characterization and modeling of particle reinforced metal matrix composites: part I

Quantitative description of microstructural morphology

M. Li ^a, S. Ghosh ^{a,*}, O. Richmond ^b, H. Weiland ^b, T.N. Rouns ^b

^a *Ohio State University, Department of Aerospace Engineering, Applied Mechanics and Aviation, 209 Boyd Laboratory, 155 West Woodruff Avenue, Columbus OH 43210, USA*

^b *ALCOA Technical Center, Pittsburgh PA 15069, USA*

Received 24 June 1998; received in revised form 16 November 1998

Abstract

In this first of a two part sequence of papers, 3-D microstructures of Si particle reinforced aluminum matrix composites are computationally constructed by assembling digitally acquired micrographs obtained by serial sectioning. The material samples considered vary in volume fraction and in particle size. Furthermore, equivalent microstructures with actual particles replaced by ellipses (in 2-D) or ellipsoids (in 3-D) are computationally simulated for efficiency. The equivalent microstructures are tessellated by a particle surface based algorithm into a mesh of Voronoi cells. Various 3-D characterization functions are developed to identify particle size, shape, orientation and spatial distribution in the actual materials and to compare with 2-D micrographs. Through this analysis, differences between 2- and 3-D characterization are established. Results indicate that it may not be sufficient to use 2-D section information for characterizing detailed microstructural features like particle shapes, orientations and near-neighbor distances. The second part of this sequence of papers will describe the important relationship of these features to damage evolution in these same materials. This sequence of papers is perhaps one of the first on 3-D physical characterization of the phase and damage structure for this class of materials. © 1999 Elsevier Science S.A. All rights reserved.

Keywords: Composites; Matrix; Microstructure; Morphology

1. Introduction

Particle and fiber reinforced composite materials have received considerable attention for use in many engineering systems due to their potential in improving mechanical properties, as well as in reducing life-cycle costs through enhanced thermomechanical stability and weight reduction. The degree of property enhancement depends on morphological factors such as volume fraction, size, shape and spatial distribution of the reinforcements, in addition to the constituent material and interface properties. Various experimental and numerical studies have established that the deformation and damage behavior of multi-phase materials can be highly sensitive to local morphology, especially by its effect on

nonhomogeneous deformation. For example, Brockenbrough et. al. [1] have concluded that the effect of fiber distribution is significant at lower volume fractions, Christman et. al. [2] have shown that clustering has a significant effect in reducing flow stress and strain hardening and Nan and Clark [3] have revealed that deformation response is affected by size, size distribution and volume fraction of particles. Using the Voronoi cell finite element model, Ghosh and Moorthy [4,5] have examined the effect of various morphologies on the damage initiation and evolution process in ductile matrix composites. In the experimental studies of Hunt and co-workers [6,7], Lewandowski and co-workers [8–16], Llorca et. al. [17], Mummery et. al. [18] and Embury and co-workers [19], the effect of particle volume fraction, size, shape, spatial distribution, material properties and stress state on deformation, damage and failure processes of ductile matrix composites are

* Corresponding author. Tel.: +1-614-2922599; fax: +1-614-2927369.

E-mail address: ghosh@osu.edu (S. Ghosh)

demonstrated. To take advantage of the improved attributes of advanced composites and to minimize failure, it is important to characterize and model microstructures for a complete understanding of the role of morphology on the deformation and damage process and prediction of component life.

Quantitative characterization with image analysis techniques is an important ingredient in predicting microstructure-property relations for heterogeneous materials. Pioneering work in quantitative metallography has been done by Richmond and co-workers [20,21], who have used Dirichlet tessellations to characterize particle geometries in steels and aluminum matrix composites by comparing actual with computer generated microstructures. Everett and co-workers [22] have determined near-neighbor distances, cell volume fractions and radial distribution functions for computer generated patterns and compared these with real materials. Pyrz et. al. [23–25] have introduced novel geometric descriptors to quantify and distinguish between various nonrandom distributions. Xi [26] has introduced the second-order autocorrelation function to characterize the spatial distribution of constituent phases based on mosaic patterns. Ghosh et. al. [27,28] have used Voronoi cell based methods as a unifying tool for characterizing and modeling the response of non-uniform multi-phase materials of arbitrary morphology.

While the aforementioned studies have been quite effective in demonstrating the importance of characterizing detailed geometry of structure, they have been essentially limited to 2-D sections of microstructures or 2-D computer models. Lewandowski and co-workers [8,11] and Lloyd [29] have characterized clustering in metal matrix composite based on Dirichlet tessellation and have shown that damage preferentially initiates in clustered regions and linkage occurs through the non-clustered regions. In [30], reference has been made to [31], which has pointed out that assessment of damage from 2-D sections can be misleading especially in the presence of particle clustering. This has also been corroborated in the experimental research with 2- and 3-D models [32]. Consequently more comprehensive 3-D examination is needed, for which few innovative methods have been suggested in the literature. A common technique is to perform microstructural characterization for 2-D section micrographs and then use stereological rules to make inference about 3-D characteristics. Stereological methods commonly estimate number density and size of 3-D objects from density and size of 2-D sections [33–36]. Methods of estimating particle surface area from plane sections are discussed in [36,33]. Saltykov [37,38] has proposed a method, by which it is possible to predict distributions of 3-D spherical size from 2-D circular section size distributions. DeHoff et. al. [39] and Cruz-Orive [40] have developed methods for generating shape and size distri-

butions of prolate or oblate spheroids from those of elliptical cross-sections. More recently Richmond and co-workers have simulated 3-D distributions from actual 2-D micrographs by pseudo-Saltykov transformation [41] and pair correlation functions [42,43]. While these stereological methods are no doubt novel, they are generally restrictive in nature. In most cases they are able to yield only a part of the morphological information and are not very effective in situations where detailed 3-D materials models are necessary.

In order to obtain detailed information on 3-D microstructures, methods of non-destructive evaluation have been proposed. One class of techniques is based on ultrasonics or its variants, such as acoustic microscopy and laser ultrasonics [44]. The laser based optical techniques, including holographic interferometry, shearography and diffracto-sight, rely on good reflection properties of the specimen and have limited applications in composites. The development of confocal microscopes with computer control has brought about the recent use of optical sectioning with 3-D image reconstruction for tissues and materials [44–46]. However, this method works well only for specimens that are at least translucent. Another method proposed recently is based on computer tomography (CT) [48]. While this technique is undoubtedly promising with recent advances in X-ray source and detector technologies, industrial high resolution CT systems are so far capable of achieving spatial resolutions only down to 25 μm . This is insufficient for capturing contours of the smaller particles and damage features in many composites such as discretely reinforced aluminum (DRA's), for which the typical particle size is less than 10 μm and the cracks are less than 3 μm . Recently Buffiere et. al [47] have developed a CT technology to yield tomographic images with a high spatial resolution ($\approx 6.5 \mu\text{m} \times 6.5 \mu\text{m} \times 6.5 \mu\text{m}$). This technique is however in a research stage and has not yet been commercialized. Alternatively, a serial sectioning method has been utilized by Weiland et. al. [49] to obtain 3-D distributions of grains for polycrystalline materials. It involves gradual removal of material layers to obtain a series of scanning electron/optical micrographs, representing sections of a microstructure. Li et. al. [32] have applied this technique to particle reinforced metal matrix composite materials to reconstruct 3-D microstructures from serial 2-D sections. This new method is inexpensive, yet highly accurate for particle and damage sizes in the 1–3 μm range.

This is the first of a two part sequence of papers that are intended for construction and characterization of microstructural morphology with respect to reinforcements and damage. In this first paper, 3-D microstructure models are first computationally constructed by sequentially assembling digital section micrographs obtained by serial sectioning. Different types of pre-

strained Si particle reinforced Al–Si–Mg matrix composites (DRA's) are analyzed. The material samples considered differ in volume fraction and particle size. The sectioning direction is transverse to the extrusion direction. Equivalent microstructures with the actual particle geometries replaced by ellipses (in 2-D) or ellipsoids (in 3-D) are computer simulated for increased efficiency. This transformation retains all essential features of the actual microstructure. The equivalent microstructures are tessellated by a surface based algorithm into meshes of Voronoi cells, each containing a particle. Various 3-D characterization functions of geometric parameters are generated to identify the particle size, shape, orientation and spatial distributions in the actual composites and are compared with similar function for 2-D micrographs. Through this image analysis, the difference in characteristics of 2- and 3-D modeling is analyzed to establish the need for the latter.

2. Experimental procedure for microstructure construction

2.1. Materials analyzed

The materials analyzed are based on an Al–Si–Mg alloy system developed at ALCOA Technical Center by Hunt [6] for studying damage evolution in metal matrix composites. This alloy system was fabricated by a powder metallurgy process. It provides model materials for which the size and volume fraction of reinforcing particles and the strength of the matrix can be varied independently. The specific systems analyzed contained approximately 10 and 20% by weight of Si particles. Depending on the heat treatment, a small portion of Si remained in solid solution or was associated with Mg in the form of Mg_2Si . The Mg level was about 0.4% by weight. Material specimens considered in this study were naturally aged and classified into three main categories, viz. (a) 10BS with 10% weight fraction of smaller Si particles, (b) 10BL with 10% weight fraction of larger Si particles, and (c) 20BL with 20% weight fraction of larger Si particles. Quantitative analyses performed with 2-D sections in [6,50] report the mean (mean) and standard deviation (S.D.) of particle diameters in the as-extruded condition as:

1. 10BS: mean = 5.12 μm and S.D. = 2.97 μm
2. 10BL: mean = 7.65 μm and S.D. = 4.81 μm
3. 20BL: mean = 7.65 μm and S.D. = 4.80 μm

The alloys were produced by rapid solidification of fine powders using a gas atomization process. Details of this procedure are discussed in [6,32] The consolidated billets were then extruded into bars of cross-section 25 mm \times 44.5 mm with an extrusion ratio of 16:1. The natural aging condition was attained through a solutionizing treatment, followed by a water quench and

finally aging at room temperature. The materials considered in this paper were deformed to 6% strain. The volume fractions of the Si particles were determined as 10.1 and 20.4% from density measurements using an immersion method.

2.2. Microstructure by serial sectioning and computer assembly

Serial sectioning is a method of gradual material removal to sequentially expose parallel layers of the microstructure in a specimen. To construct 3-D microstructures of the particle reinforced aluminum matrix composites, this method is first used to generate a series of section micrographs showing details of microstructural morphology (see Fig. 2a). While this process is tedious, it remains the best known method for accurate 3-D visualization, image analysis, and microstructure reconstruction at the required resolution of particle size and spacing ($\approx 5 \mu m$). A unique feature of the process is that the step size or depth of material removal per pass can be controlled according to the desired scale of microstructural features.

As discussed in [32], parallel layers are removed using a precision dimple grinder. The depth of material removal per step is selected such that each particle is sectioned at least once, ensuring that all particles of interest are adequately captured in the micrographs. For example, the particle size range for the 10 and 20BL materials is approximately 3–23 μm , with an average size of $\approx 8 \mu m$. The section to section step size is chosen to be 2.75 μm , corresponding to a total thickness of 55 μm for 20 sections. For the 10BS material, the particle size range is 1.5–17 μm , with an average size of $\approx 4 \mu m$. The chosen step size is 1.5 μm corresponding to a total thickness of about 30 μm for 20 sections. Larger particles yield multiple sections revealing more information on their 3-D geometry. Images of 2-D micrographs of each section are digitized as shown in Fig. 1(a). They are then serially stacked on a computer to yield 3-D microstructures as shown in Fig. 2(a), with the help of two software packages [51,52] for graphic analysis of 3-D volumetric data and for analyzing image data. The precise 3-D location, shape, size and orientation of each particle can be obtained at a fairly high resolution ($\approx 5 \mu m$ for the materials considered) by this method. Details of the serial sectioning process are presented in [32].

3. Equivalent microstructure and its discretization

3.1. Generating the equivalent microstructure

The actual 3-D geometry of particles in metal matrix composites, as seen in Fig. 2(a), can be quite complex

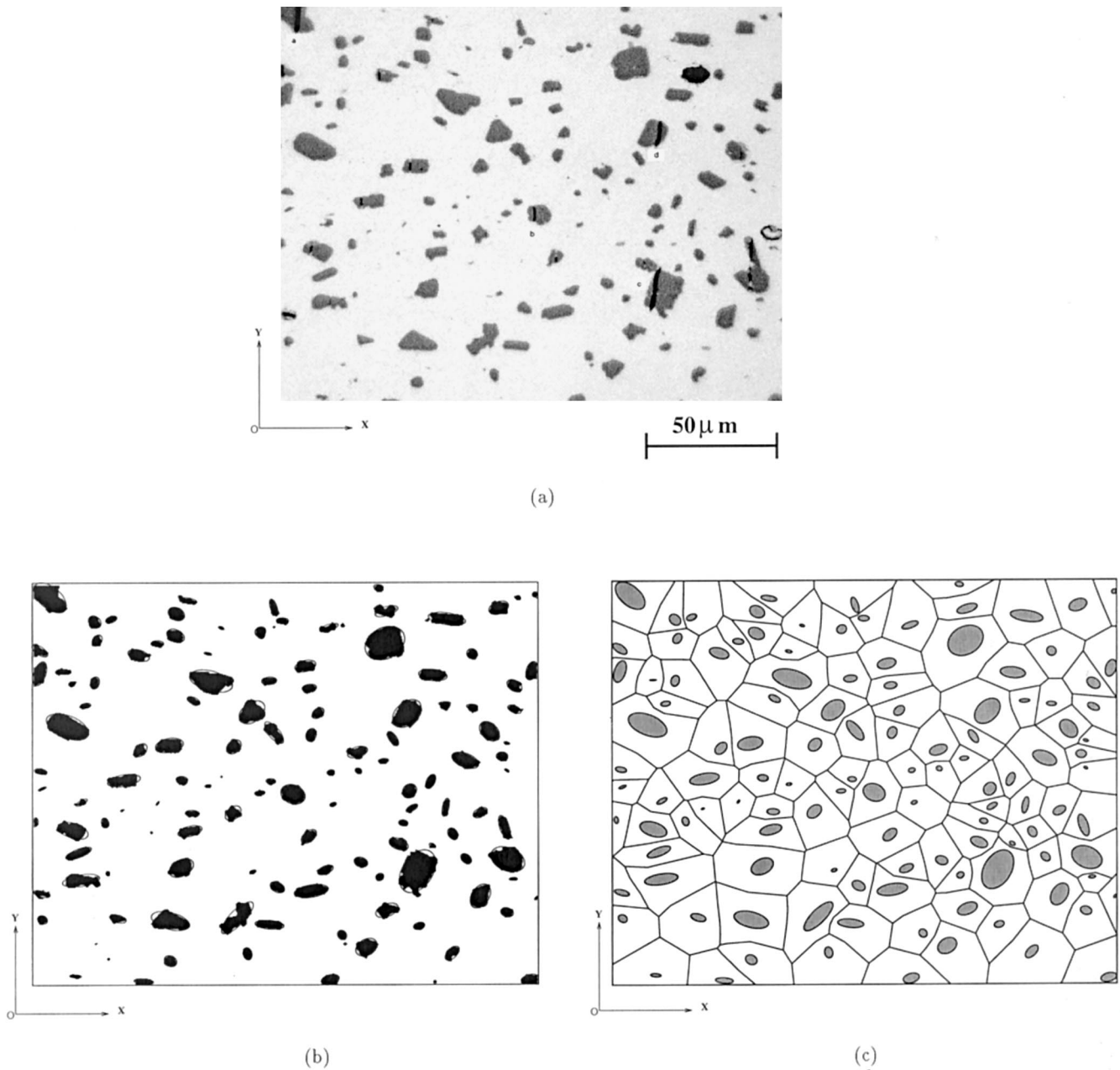


Fig. 1. (a) Optical micrograph of a section of 10BL Al–Mg–Si composite ($\text{Si } V_f = 10\%$). (b) Simulated microstructure superimposed on the micrograph. (c) Two dimensional Dirichlet tessellation of the microstructural domain.

and an exhaustive database is required to store all geometric details. To avert this, equivalent microstructures that closely approximate the actual morphology but are computationally less demanding, are generated. In this process, each particle is replaced by an equivalent ellipse (in 2-D) or ellipsoid (in 3-D). This process economizes the image analysis and characterization process by way of well known geometric properties. For obtaining equivalent microstructures, digitized image data is first transferred into a binary format to distinguish between the particle and matrix phases. The zero

(I_0), 1st (I_x, I_y) and second (I_{xx}, I_{yy}) order geometric moments are then computed for each particle by adding contributions from each voxel (in 3-D) or pixel (in 2-D) that lies within the particle boundary. For 2-D microstructures the computed moments are equated to the moment formulae for ellipses to evaluate the centroidal coordinates (x_c, y_c), half major and minor axis lengths (a, b), and orientation θ of the major axis from:

$$x_c = \frac{I_y}{I_0}, \quad y_c = \frac{I_x}{I_0} \quad (1a)$$

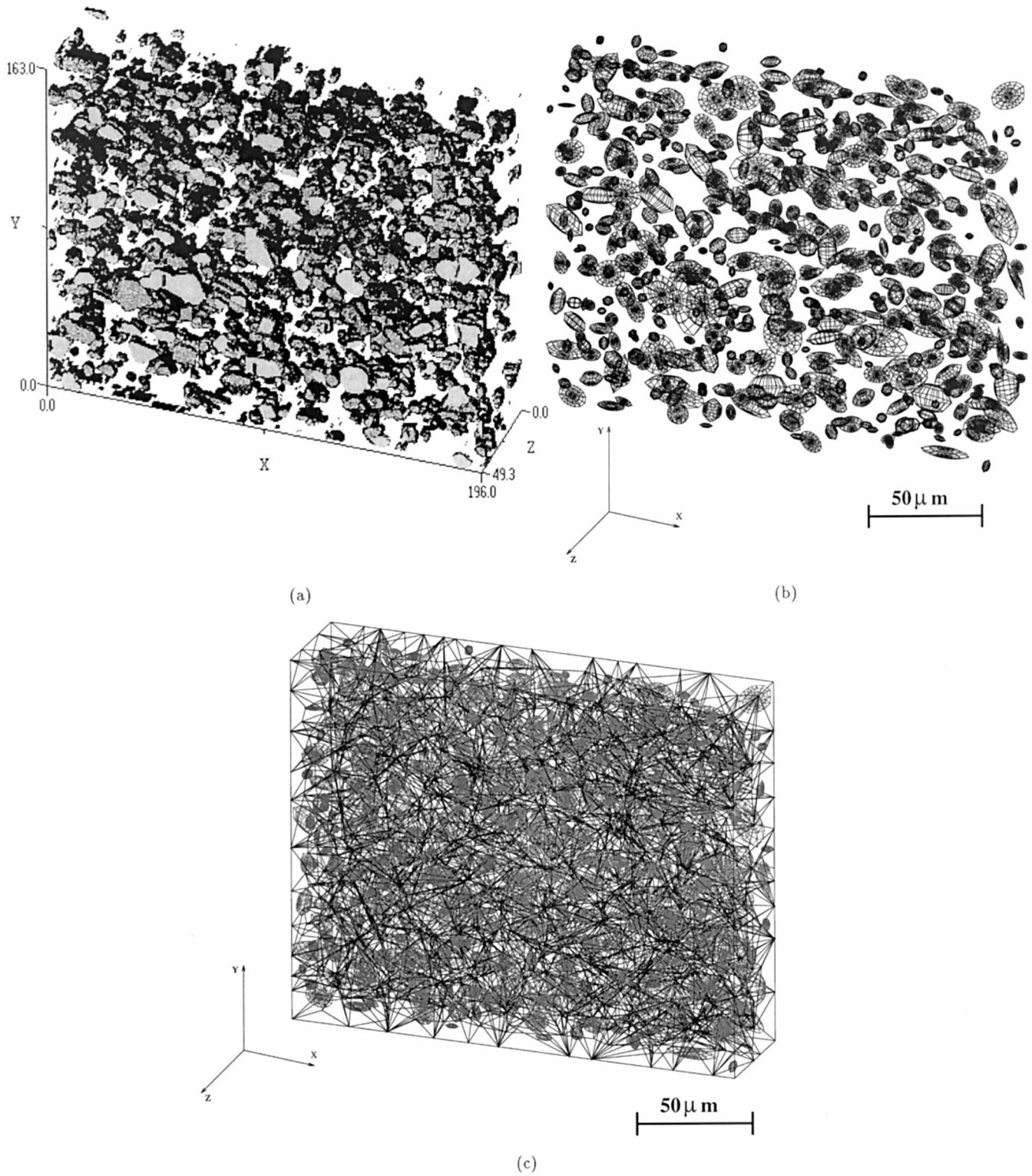


Fig. 2. (a) Three dimensional microstructure from serial-sectioning. (b) Simulated equivalent microstructure with ellipsoidal inclusions. (c) Tessellation microstructural domain with Voronoi cells for a 10BL Al–Mg–Si composite (units are in μm).

$$a = \sqrt{\frac{1}{2}(C_1 + \sqrt{C_1^2 - 4C_2})},$$

$$b = \sqrt{\frac{1}{2}(C_1 - \sqrt{C_1^2 - 4C_2})} \quad (1b)$$

Table 1
Particle statistical parameters^a

MGRP	MA (SDA)	MD (SDD)	ML (SDL)	MAR (SDAR)	AF (%)	NP
10BL-Sec1	24.90 (28.34)	4.964 (2.657)	6.794 (3.738)	1.915 (0.566)	9.77	119
10BL-Sec3	27.94 (39.19)	5.131 (3.042)	7.166 (4.446)	1.941 (0.721)	10.48	114
10BL-Sec5	31.06 (41.41)	5.325 (3.345)	7.334 (4.792)	1.917 (0.662)	10.74	105
10BL-Sec8	27.34 (30.37)	5.141 (2.894)	7.108 (4.148)	2.003 (0.946)	10.16	113
10BL-Sec10	21.44 (24.09)	4.584 (2.508)	6.363 (3.894)	2.007 (1.043)	9.25	131
10BL-Sec13	23.13 (25.91)	4.737 (2.649)	6.579 (4.227)	2.035 (1.129)	8.75	115
10BL-Sec15	24.05 (27.22)	4.869 (2.629)	6.701 (4.429)	1.876 (0.830)	7.83	99
10BL-Sec18	29.16 (34.01)	5.292 (3.019)	7.254 (4.516)	1.962 (1.123)	10.75	112
10BL-Sec20	32.13 (35.35)	5.648 (3.003)	7.697 (4.317)	1.931 (0.693)	9.75	106
10BL-3-D	204.8 (363.1)	6.045 (2.772)	8.215 (4.103) 1	2.670 (1.242)	8.97	634
10BS-3-D	107.4 (102.9)	5.466 (1.525)	6.574 (2.671)	3.168 (1.249)	7.48	672
20BL-3-D	197.9 (321.1)	5.941 (2.816)	8.142 (4.529)	3.091 (1.460)	15.10	741

^a Abbreviations: (MA, SDA), mean and standard deviation of particle area/volume in $\mu\text{m}^2/\mu\text{m}^3$; (MD, SDD), mean and standard deviation of particle equivalent diameter in μm ; (ML, SDL), mean and standard deviation of major axis length in μm ; (MAR, SDAR), mean and standard deviation of aspect ratio; (AF), total area/volume fraction for particles; (NP), number of particles.

$$\theta = \frac{1}{2} \cos^{-1} \left(\frac{4}{a^2 - b^2} \right) \left(\frac{I_{yy} - I_{xx}}{I_0} - \frac{I_y^2 - I_x^2}{I_0^2} \right) \quad (1c)$$

where

$$C_1 = 4 * \left(\frac{I_{xx} + I_{yy}}{I_0} - \frac{I_x^2 + I_y^2}{I_0^2} \right)$$

and $C_2 = I_0^2/\pi^2$. In some materials with high volume fractions and clustering, it is likely that the equivalent ellipses may overlap. In this event, adjustment factors are introduced to locally reduce the size of one ellipse and avoid penetration. Fig. 1(b) shows an equivalent microstructure superimposed on the actual micrograph of Fig. 1(a) for a section of the 10BL composite. Fairly good concurrence with the micrograph, in terms of important morphological features, is obtained.

For 3-D microstructures, the centroidal coordinates (x_c, y_c, z_c) of the equivalent ellipsoid are first evaluated from the zero and first order moments as:

$$x_c = \frac{I_y}{I_0}, \quad y_c = \frac{I_x}{I_0}, \quad z_c = \frac{I_z}{I_0} \quad (2)$$

The principal directions (or orientations of the three axes) for the ellipsoids are obtained from the eigen-values of the second order moments I_{ij} ($i = 1, \dots, 3$, and $j = 1, \dots, 3$). The major ($2a$), intermediate ($2b$) and minor ($2c$) axes of the equivalent ellipsoids are then obtained from the principal moments I_1, I_2, I_3 as:

$$a = \sqrt{\frac{5}{I_0}(I_2 + I_3 - I_1)} \quad (3a)$$

$$b = \sqrt{\frac{5}{I_0}(I_1 + I_3 - I_2)} \quad (3b)$$

$$c = \sqrt{\frac{5}{I_0}(I_1 + I_2 - I_3)} \quad (3c)$$

A computer simulated 3-D equivalent microstructure

for the 10BL Al–Mg–Si composite is shown in Fig. 2(b). Three dimensional volume fractions, 2-D area fractions, and the number of particles in each of the equivalent microstructures are presented in Table 1. Due to the large number of heterogeneities in each section, contributions from particles below a pre-determined lower limit size are ignored. In this paper, this limit is set at around half the mean particle size. This causes a small discrepancy between some experimentally reported and computed statistical parameters.

3.2. Discretization into Voronoi cells

Voronoi tessellation is defined as subdivision of a region, determined by a set of points, such that each point has associated with it a region that is closer to it than to any other. The subdivided regions are called Voronoi cells. Tessellation into a mesh of Voronoi cells plays an important role in developing geometric descriptors for quantitative characterization. The cells may be identified with basic structural elements in a heterogeneous microstructure. They represent regions of immediate influence for each heterogeneity and also define neighbor regions by the cell facets. This facilitates easy evaluation of parameters like local area fractions, near neighbor and nearest-neighbor distances and orientations.

When the germinating points are replaced by heterogeneities with shape, size and orientation, the discretization should account for these features and avoid intersection of the Voronoi cell edges with the heterogeneities. A two dimensional mesh generator has been developed for plane sections of multiphase materials in Ghosh and Mukhopadhyay [53]. In this paper, effects of shape, size and orientation of the ellipses are accommodated through a surface based algorithm, where the surface of a heterogeneity is represented by an adequate

number of points. The corresponding Voronoi cell edges are generated as perpendicular bisectors of lines joining nearest surface points on two adjacent heterogeneities. A smoothing process is implemented to replace groups of small line segments by a single line without intersecting the generating heterogeneities. A tessellated micrograph with a mesh of 2-D Voronoi cells is shown in Fig. 1(c).

For the 3-D microstructures, two surface points on a pair of ellipsoidal particles, corresponding to the nearest surface-to-surface distances are determined by solving a constrained minimization problem. Bisector planes that are perpendicular to the lines joining these nearest points are then generated. Intersections of these bisector planes constitute the edges, and intersections of edges form the vertices of the resulting Voronoi cells. Special precautions and measures are taken to avoid problems of overlapped Voronoi polyhedra or voids between them, by collapsing undesirable vertices onto suitably chosen common points. A tessellated mesh of 3-D Voronoi cells for the 10BL Al–Mg–Si composite is shown in Fig. 2(c).

4. Quantitative characterization

Microstructural morphology for heterogeneous materials is suitably characterized by various functions of shapes, sizes and spatial distributions of the constituent phases. Studies in quantitative metallography by Richmond et. al. [20,21], Pyrz [23,24], Hunt [6], Everett [22] and Ghosh et. al. [27,28] have suggested different classifier functions and methods as a means for characterizing microstructural morphology. This paper extends these studies to the analysis of actual 3-D composites microstructures as well as their 2-D sections. Comparison of the 2- and 3-D results are made with well known statistical formulae and also with results of stereology e.g. the Saltykov transformation (ST) [37] and the Cruz-Orive method [40].

4.1. Particle geometry

4.1.1. Mean and standard deviations

Various statistical parameters related to particle size in micrographs of 2-D sections of 10BL composites and 3-D microregions of the 10BL, 10BS and 20BL composites are presented in Table 1. MA (SDA) corresponds for the mean (standard deviation) of particle areas/volumes; MD (SDD) is the mean (standard deviation) diameters (EQS) of equivalent circles or spheres having the same areas or volumes, i.e.

$$EQS = 2 * \left(\frac{\text{area}}{\pi} \right)^{1/2} \quad \text{in 2D and}$$

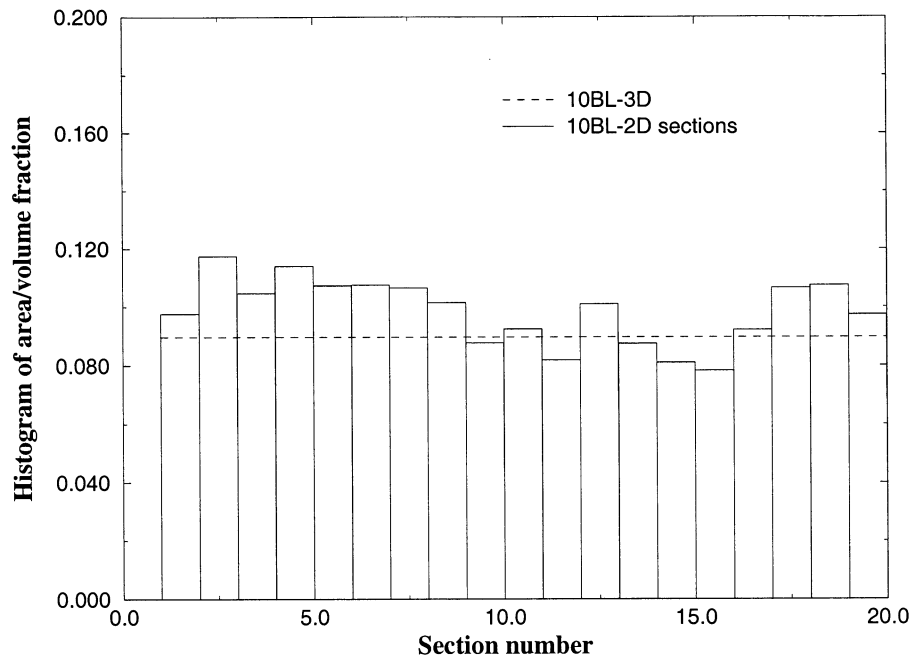
$$EQS = \left(\frac{3}{4\pi} * \text{volume} \right)^{1/3} \quad \text{in 3D;}$$

ML (SDL) are the mean (standard deviation) lengths of the major axes of ellipses or ellipsoids; MAR (SAR) are the mean (standard deviation) aspect ratios; AF is the total particle area or volume fraction; and NP corresponds to the total number of particles in the microregion analyzed.

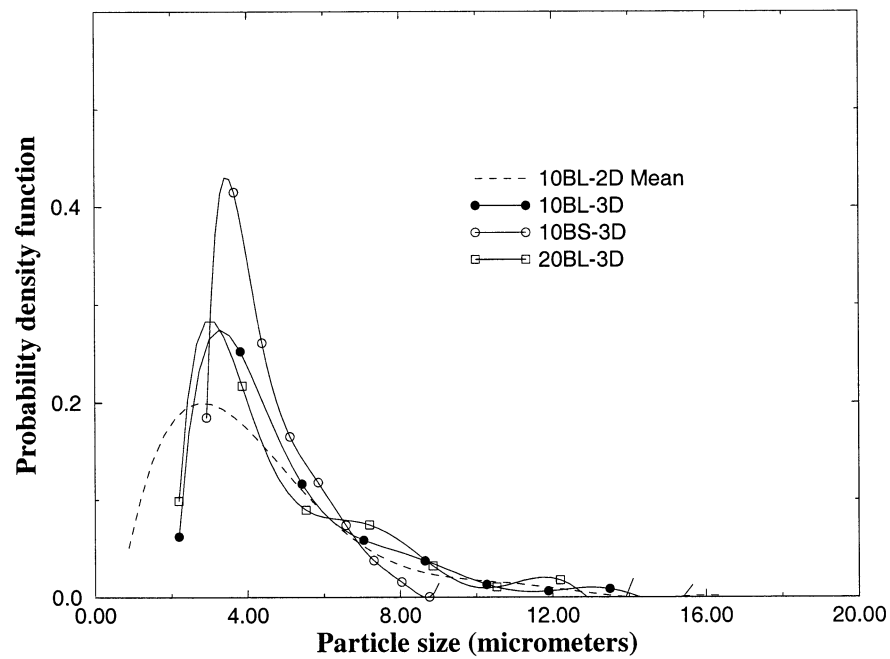
Particle size is assessed from equivalent diameters (MD) and major axis lengths (ML) in Table 1. There is a considerable scatter of particle sizes observed in the 2-D sections, viz. $\approx 20\%$ in MD and $\approx 17\%$ in ML, implying non-uniformity in the transverse direction. Furthermore, the relatively high values of standard deviation correspond to significant variation in the particle sizes within each section. Three dimensional particle sizes are in general larger than those in 2-D sections. This results from the fact that the section planes may not coincide with the principal planes with the largest dimensions, even though the sections are parallel to the extrusion direction. Aspect ratios (MAR) for the 2-D sections are approximately within 8% of each other and are smaller than the 3-D aspect ratios. Thus the smallest principal directions of the ellipsoids may be at angles to the section planes. However, since the extrusion direction is perpendicular to the sectioning direction, the largest principal directions may lie in the section planes. The AF and NP show considerable variation in the third direction. During the sectioning operation in [32], some sections are observed to be harder than others. This may be attributed to the variation in particle area fraction in the transverse direction. For the three materials considered, the results verify that the 10BL and 20BL composites possess larger size particles (larger MA, MD and ML) than the 10BS composite, but the aspect ratio is larger for the 20BL and 10BS composites.

4.1.2. Size effects

Histograms of the total area fraction of the 2-D sections and the corresponding 3-D volume fraction for the 10BL composite are plotted in Fig. 3(a). Reasonable variation in the total area fraction about the volume fraction is observed. The probability density functions $f(EQS)$ of the equivalent size ($f(x) = (dF(x)/dx)$), where $F(x)$ represents the cumulative distribution function and $f(x)$ is the probability of X assuming the value x) for the mean of all 10BL composite sections and 3-D microregions of the 10BL, 10BS and 20BL composites are plotted in Fig. 3(b). There is considerable difference between the 2- and 3-D plots of the probability functions, though most of the 2-D sections themselves exhibit very similar behavior and are tightly packed in narrow bands. The smallest particle sizes, reflected by starting values of the plots, are smaller for 2-D than



(a)



(b)

Fig. 3. Particle size characterization: (a) histogram of total area fraction of 2-D sections compared with the 3-D volume fraction for the 10BL composite; (b) probability density functions of particle size (equivalent diameter) for various sections of 10BL microregions of 10BL and 3-D microregions of 10BL, 10BS and 20BL composites.

for 3-D. Peaks in probability density, which correspond to the most probable sizes, occur at values lower than the mean size. The peak for 10BS composite is higher than those for the 10BL and 20BL composites, indicating a larger size concentration in this range. The largest particle size extends up to about 16 μm for the 10BL material.

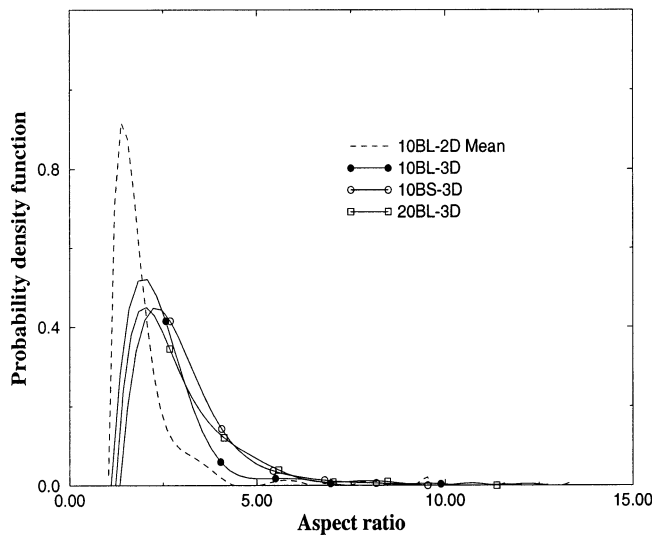
4.1.3. Shape effects

The probability density functions of aspect ratio $f(AR)$ for the mean of various sections of the 10BL material and the 3-D microstructures of 10BL, 10BS and 20BL materials are plotted in Fig. 4(a). For all 2-D sections, aspect ratios are found to exhibit very similar

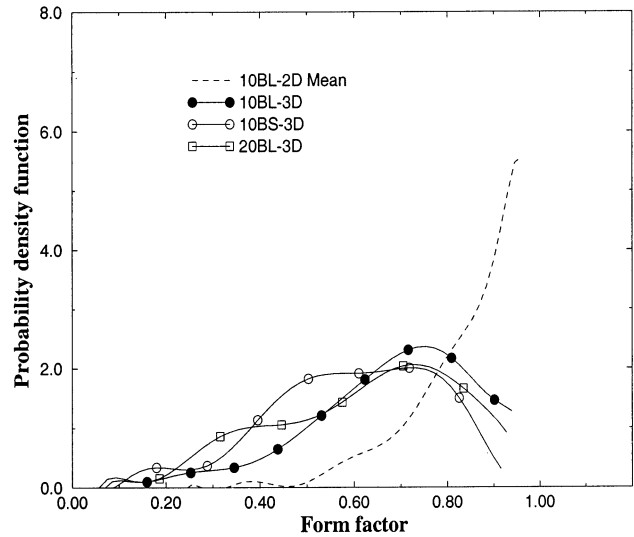
variation and $f(AR)$ plots are closely packed. The 2-D sections however, exhibit higher peaks at lower values of aspect ratios in comparison with 3-D. This infers a larger concentration of equiaxed or lower aspect ratio for the 2-D sections. While the $f(AR)$ distributions are wider for 3-D than for the 2-D sections, the behavior for all three materials are similar. A second way of characterizing shapes is through a form factor defined as [35]:

$$\text{Form factor} = \frac{4\pi A}{P^2} \quad \text{in 2D and} \quad \frac{36\pi V^2}{SF^3} \quad \text{in 3D} \quad (4)$$

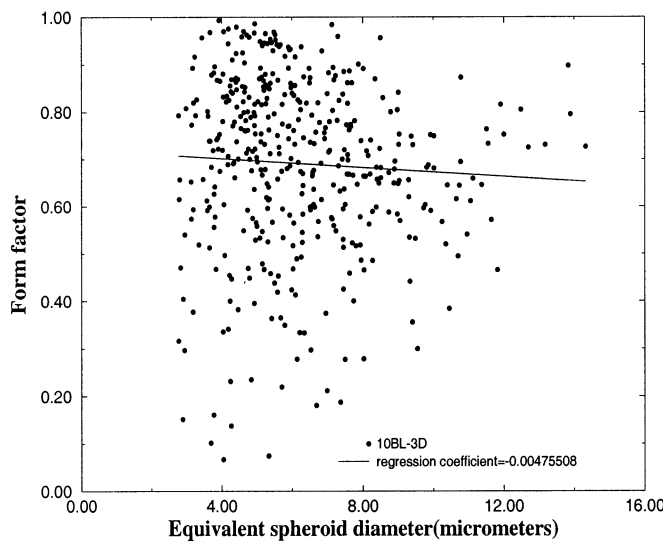
where A, P, V, SF correspond to the area, perimeter, volume and surface area respectively. For an ellipse with major and minor axes lengths $2a$ and $2b$, the area is ($A = \pi ab$) and the perimeter is approximated as ($P = \pi(1.5(a + b) - \sqrt{ab})$). For an ellipsoid with axes



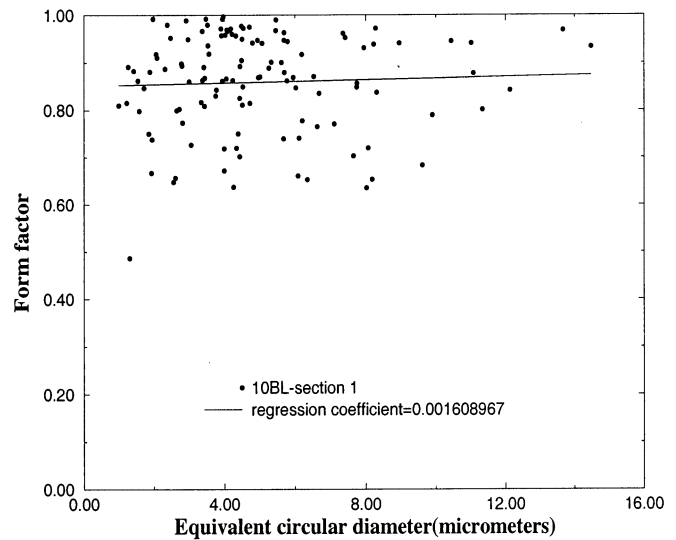
(a)



(b)



(c)



(d)

Fig. 4. Particle shape characterization: (a) probability density function of aspect ratio; (b) probability density functions of form factor for various sections of 10BL and 3-D microregions of 10BL, 10BS and 20BL composites; (c) 3-D form factor vs. size (equivalent diameter) for 10BL composite; (d) section form factor vs. size (equivalent diameter) for a section of 10BL composite.

length $2a$, $2b$ and $2c$, the volume is ($V = \frac{4}{3}\pi abc$) and the surface area is:

$$\left(SF = 2\pi c^2 + \frac{2\pi b}{\sqrt{a^2 - c^2}}(c^2 F(k, \varphi) + (a^2 - c^2)E(k, \varphi)) \right)$$

where

$$k = \frac{a}{b} \sqrt{\frac{b^2 - c^2}{a^2 - c^2}}, \quad \varphi = \cos^{-1}\left(\frac{c}{a}\right)$$

and $F(k, \varphi)$, $E(k, \varphi)$ are elliptic integrals of the first and second kinds. The dimensionless form factor is unity for a perfect circle or sphere and decreases in value with increasing shape irregularity. The probability density functions $f(F)$ of form factors are plotted in Fig. 4(b). The variation of $f(F)$ resembles a reflected image of $f(AR)$ in Fig. 4(a). This is because the form factor varies from 1 for equiaxed to low values for higher aspect ratio particles, while the aspect ratio varies from 1 for equiaxed particles to higher values. The $f(F)$ plots for 3-D have less pronounced peaks at values other than unity in comparison with the 2-D sections. This shows that actual microstructures have a wider distribution of irregular shapes than is inferred from 2-D sections. Form factors are also plotted as functions of equivalent diameters in Fig. 4(c) and (d). A linear regression analysis is used to express the dependence of form factor on size, with regression coefficient depicted by the slope. The scatter in form factor is more for 3-D with a mean of ≈ 0.75 , which is smaller than the 2-D mean (≈ 0.83). This again confirms shape irregularity in 3-D particles. The scatter is larger at smaller sizes. The regression coefficients are small implying that the form factor is not a strong function of particle size.

4.2. Stereological methods in size and shape distributions

A number of stereological methods have been proposed to estimate various attributes of 3-D geometric constructs from 2-D section data e.g. [41–43]. In the present work, the ST method [37] and its derivatives are employed to simulate 3-D particle distributions from data on section micrographs and also to compare statistics with 3-D microstructures. The method proposed in [37] is for spherical geometries with circular cross-sections. Consequently, the stereological method uses equivalent circular diameters EQS of each particle contour in the micrographs for constructing 3-D distributions. The full range of particle diameters in a microstructure is divided into m intervals of length $\Delta = D_{\max}/m$ each, where D_{\max} is the largest diameter. The method assumes that the diameter of the largest sphere is equal to that of the largest circle in the section, and also that both 2- and 3-D size ranges are

divided into the same number of identical intervals. With these assumptions, the 3-D particle size distribution is projected from a 2-D size distribution as:

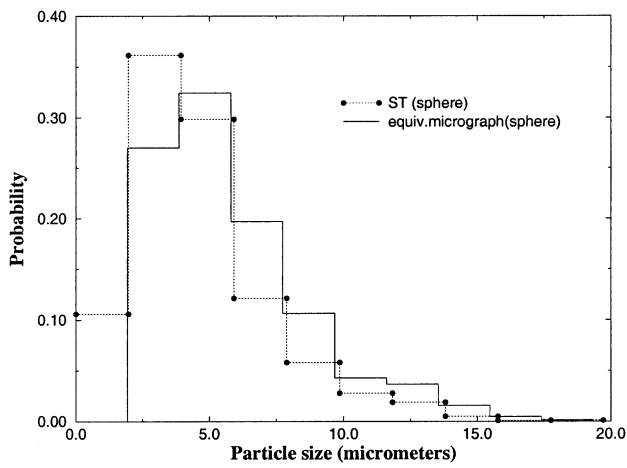
$$N_V(j) = \frac{1}{\Delta} \sum_{i=j}^m \alpha_{ij} N_A(i) \quad (5)$$

where $N_V(j)$ is the number of spheres in the j th size interval, $N_A(i)$ is the number of 2-D cross-sections in the i th size interval and α_{ij} are stereological coefficients presented in Weibel [33]. In the construction of 3-D size distributions by the ST method, the statistics of all sections from the serial sectioning operation are considered. Results for the 10BL composite are plotted in Fig. 5. The histogram of probability distributions in Fig. 5(a), correspond to the cumulative probability that a parameter lies within a given range i.e. $P(a < X \leq b)$. Fig. 5(b) shows the corresponding volume fraction as a function of the equivalent diameter EQS . Particle volumes for each interval in the ST method are calculated by using the mean value of diameter for that interval, e.g. $(i - 1/2)\Delta$ for the i th interval. While the size distributions are generally in good agreement in Fig. 5(a), the Saltykov method shows a higher distribution at smaller sizes. This may in part be due to the fact that some of the smaller particles in the ellipsoidal simulation are discarded. This effect is not as appreciable for the volume fraction distribution in Fig. 5(b), where results of stereology and the actual microstructure agree rather well.

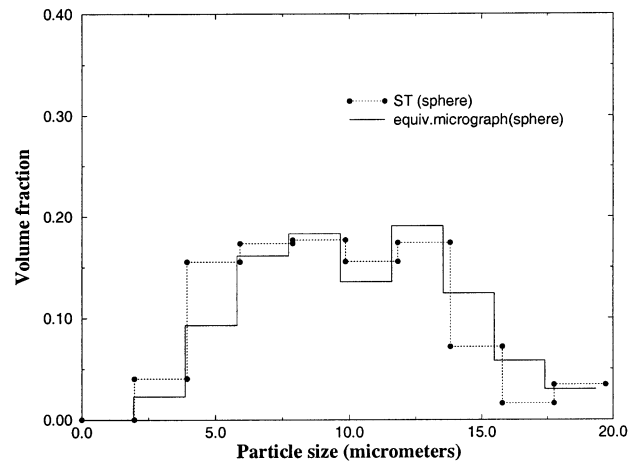
A modified version of the Saltykov method (MST) incorporating shape effects has been suggested by Cruz-Orive [40] for generating prolate or oblate spheroid geometries from known distributions of elliptic cross-sections. The lengths of the major axis $a \leq A$ and minor axis $b \leq B$ for each elliptical section is first recorded for constructing these spheroids. A and B correspond to the maximum major and minor axis lengths for each micrograph. As with the ST method, the range of 2-D ellipses and the 3-D spheroids are divided into m intervals or classes. The size of these intervals are based on the largest minor axis size B for prolate spheroids and the largest major axis size A for oblate spheroids. Thus for prolate spheroids $\Delta B/m$ and for oblate spheroids $\Delta = A/m$. In addition, a shape parameter (or square eccentricity) is defined as $y^2 = 1 - (b/a)^2$. The range of $y^2 \in (0, 1)$ was also divided into k intervals of equal size $1/k$. 2- and 3-D objects with sizes between $[(i - 1)\Delta$ and $i\Delta]$, and shape parameter y^2 between $[(j - 1)/k$ and $j/k]$ belong to the (ij) th size–shape interval. The 3-D spheroid size–shape distribution is then obtained from the 2-D size–shape distribution [40] as:

$$N_V(i, j) = \frac{1}{\Delta} \sum_{\alpha=i}^s \sum_{\beta=j}^k p^{i\alpha} N_A(\alpha, \beta) q^{j\beta} \quad (6)$$

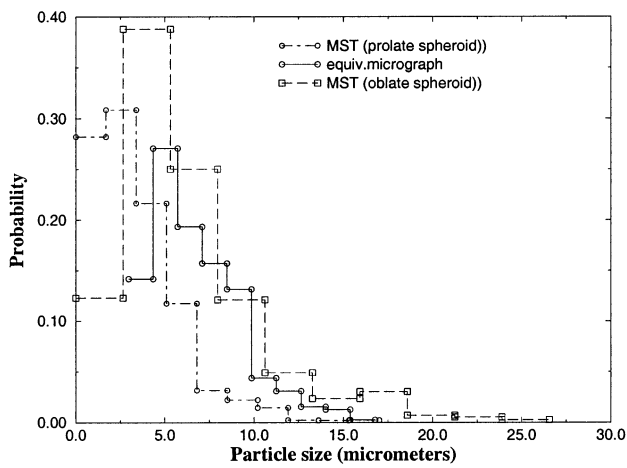
where $N_V(i, j)$ is the number of prolate or oblate spheroids in the ij th size–shape interval and $N_A(\alpha, \beta)$ is



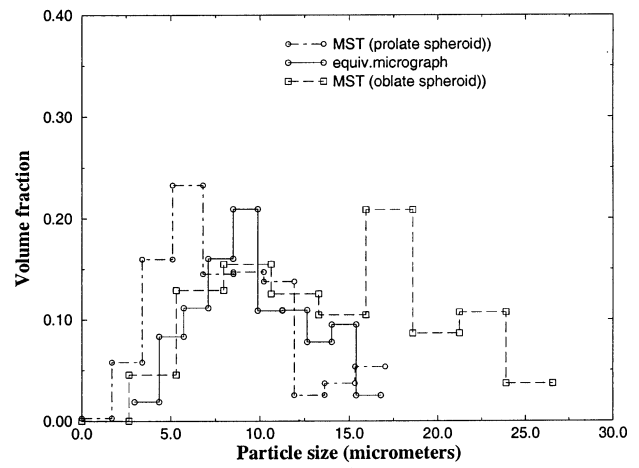
(a)



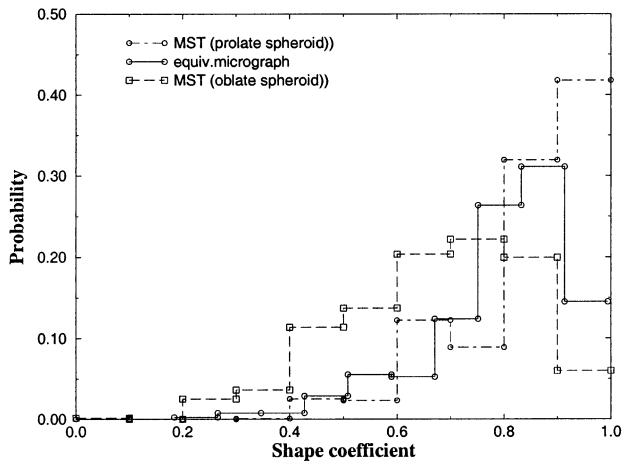
(b)



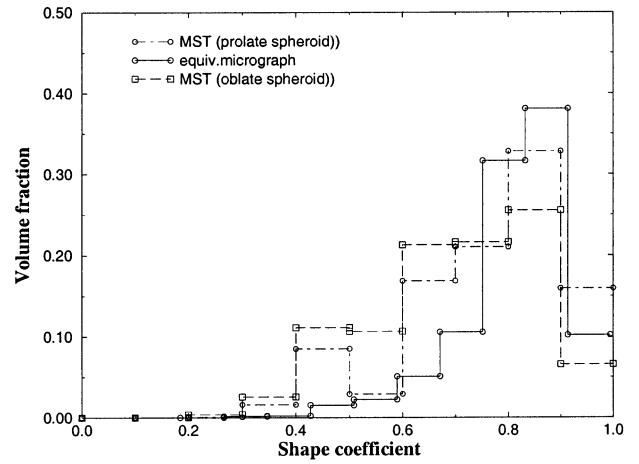
(c)



(d)



(e)



(f)

Fig. 5. Distribution functions for 10BL computed by ST method: (a) probability distribution of particle size (diameter) for equivalent spheres (ST); (b) volume fraction vs. particle size for equivalent spheres (ST); (c) probability distribution of particle size for equivalent spheroids (MST); (d) volume fraction vs. particle size for equivalent spheroids (MST); (e) probability distribution of particle shape for equivalent spheroids (MST); (f) volume fraction vs. particle shape for equivalent spheroids (MST).

the number of ellipses in the size–shape class $\alpha\beta$. The coefficients $p^{i\alpha}$ and $q^{\beta j}$ for the prolate and oblate categories are tabulated in [33].

Fig. 5(c–f) are histograms of the probability distributions and volume fractions of the particle size (a for oblate spheroids and b for prolate spheroids) and shape

coefficient y^2 , respectively, generated by the MST method. Particle volumes for each interval ij are obtained from the mean size $(i - 0.5)\Delta$ and mean shape parameter $(j - 0.5)/k$ for this interval. Results are compared with those for the 3-D microstructures generated from serial sectioning. The effective particle size for ellipsoidal particles with principal axes a , b and c ($a \geq b \geq c$), is taken to be $(a + b + c)/3$ and the shape parameter is taken as $y^2 = 1 - (c/a)^2$. Qualitative comparisons of size and shape distributions, between stereologically generated and actual microstructures with ellipsoidal particles are readily made from these figures. While differences exist, the statistics for prolate spheroids are in better agreement with the ellipsoidal particles than those for oblate spheroids. Such observations, that most particles in these composite microstructures are closer to prolate than oblate spheroids, have been also made in Hunt [6].

To gauge the effectiveness of size distributions predicted by stereology as shown in Fig. 5(a) and (c), an effectively ratio is proposed and computed as:

$$\frac{(MPF)_{st} + 3*(SDPF)_{st}}{(MPF)_{sm} + 3*(SDPF)_{sm}} = 1.0539 \quad \text{for sphere by ST}$$

$$\frac{(MPF)_{st} + 3*(SDPF)_{st}}{(MPF)_{sm} + 3*(SDPF)_{sm}} = 1.0713$$

for prolate spheroid by MST

$$\frac{(MPF)_{st} + 3*(SDPF)_{st}}{(MPF)_{sm} + 3*(SDPF)_{sm}} = 1.1841$$

for oblate spheroid by MST

Subscripts st and sm correspond to plots for microstructures generated by stereology and serial sectioning respectively. MPF and $SDPF$ are the mean and standard deviations of the probability distribution functions for spheres in Fig. 5(a), and for prolate and oblate spheroids in Fig. 5(b). For a 'normal' distribution, the terms $MPF + 3*SDPF$ appearing in the effective ratio are expected to be 99.75% of all particle sizes. From this study with the ST and MST stereological methods, it appears that the method based on size alone (ST) is more effective than that based on shapes for these materials. This conclusion is however based on very limited data and more experiments are needed for making definite claims.

4.3. Spatial distribution patterns

To classify spatial distribution, it is important to identify functions and methods that can distinguish between regular, random, non-regular, non-random or clustered patterns. A number of these functions used in [27,28] for classifying computer generated patterns are implemented in this study for real micrographs.

4.3.1. Second order statistics

Second order statistics of spatial distributions are captured by the second order intensity function $K(r)$. It has been demonstrated to be an informative descriptor of morphological patterns by Pyrz [23,24], because of its sensitivity to local perturbations in otherwise similar distributions. It has the significance of a radial distribution function and is defined as the number of additional points or inclusion centres expected to lie within a distance r of an arbitrarily located point, divided by point density. For observations within a finite window W of area A_w , $K(r)$ corrected due to edge effects is expressed as (see [23,27]):

$$K(r) = \frac{A_w}{N^2} \sum_{k=1}^N \frac{I_k(r)}{R_p} \quad (7)$$

where N is the number of points in W , $I_k(r)$ is the number of points in the circle with center at one of the points and radius r , and R_p is a compensating factor for the bounded domain that is obtained as the ratio of circumference of a circle of radius r inside W to the entire circumference. For a homogeneous Poisson distribution of points,

$$K(r) = \pi r^2 \quad \text{in 2D, and} \quad K(r) = \frac{4}{3} \pi r^3 \quad \text{in 3D.} \quad (8)$$

Correspondingly, a transformation function $L(r)$ may be defined as:

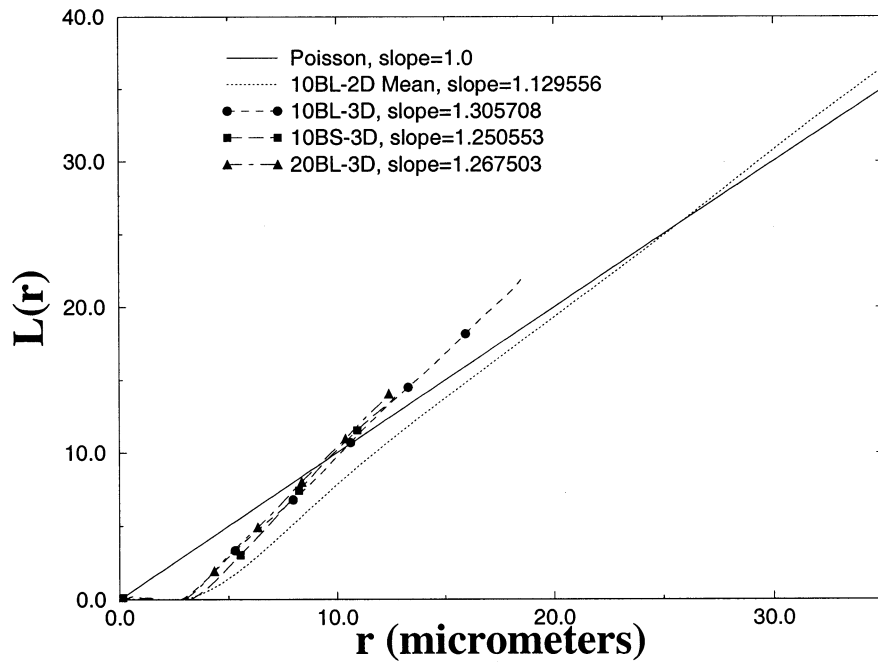
$$L(r) = \left(\frac{K(r)}{\pi} \right)^{\frac{1}{2}} \quad \text{in 2D, and} \\ L(r) = \left(\frac{3}{4\pi} K(r) \right)^{\frac{1}{3}} \quad \text{in 3D} \quad (9)$$

Thus the plot of $L(r)$ versus r is a 45° straight line for a pure Poisson distribution. It is often used as a graphical tool for detecting departures from a homogeneous Poisson process [54]. Contrary to $K(r)$ and $L(r)$ that discriminate between patterns, the pair distribution function $g(r)$ is a good quantifier of the probable occurrence of near-neighbor distances. It corresponds to probability $g(r)dr$ of finding an additional point within a circle of radius dr and centered at r , where two points are located at $r = 0$ and $r = r$, respectively, and is mathematically expressed as:

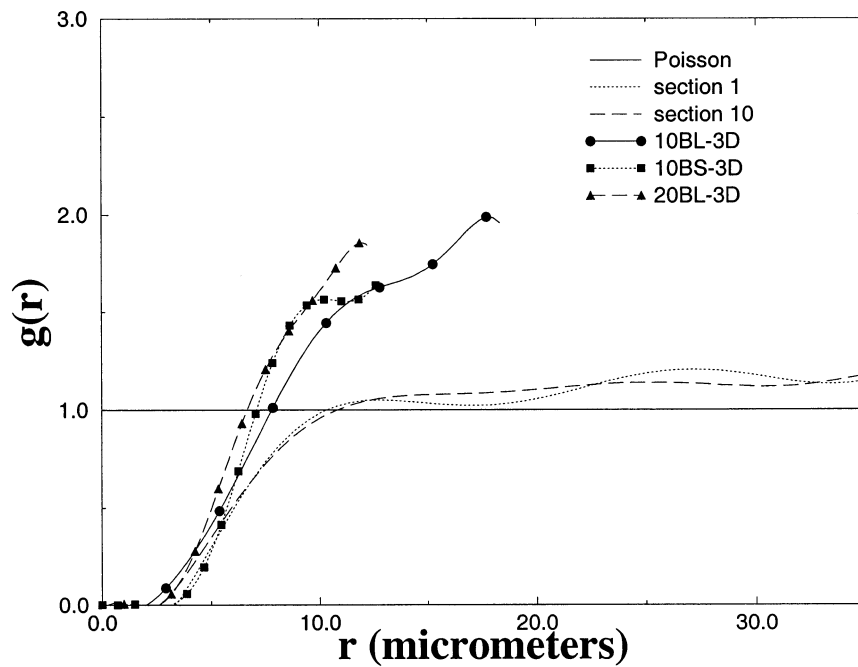
$$g(r) = \frac{1}{2\pi r} \frac{dK(r)}{dr} \quad \text{in 2D and} \quad g(r) = \frac{1}{4\pi r^2} \frac{dK(r)}{dr} \\ \text{in 3D} \quad (10)$$

For a pure Poisson pattern, $g(r) = 1$ signifying equal probability in occurrence of near-neighbor distances.

The $L(r)$ and $g(r)$ functions for the mean of 10BL composite sections and 3-D microregions of the 10BL, 10BS and 20BL composites are plotted in Fig. 6. The $L(r)$ functions in Fig. 6(a) for all the 3-D microstruc-



(a)



(b)

Fig. 6. (a) $L(r)$ and (b) $g(r)$ functions for 2-D sections and 3-D microstructures.

tures exhibit close proximity to each other implying similar spatial distributions. The functions for all 2-D sections are also close to each other. While the 3-D distribution shows a larger departure from the homogeneous Poisson pattern, the slope deviations are not sizable enough to warrant significant clustering in the microstructure. The inference of non-clustered patterns is further substantiated in the plot of the $g(r)$ functions

in Fig. 6(b). The peaks in $g(r)$ are not very pronounced and have relatively low deviations from unity. The randomness in spatial pattern is expected from the fabrication process. The highest peaks in $g(r)$ and the maximum deviation from the line $(L(r)/r)=1$ are observed for the 20BL materials. This departure from the Poisson distribution is naturally expected with increasing particle size and volume fraction. The functions

Table 2
Local measures characterizing the microstructure^a

MGRP	MAF (SDAF)	MSND (SDSND)	QS	RS	MCND (SDCND)	QC	RC
10BL-Sec1	0.0866 (0.0639)	5.3924 (3.318)	0.6749	0.6313	10.463 (3.566)	1.3095	0.7291
10BL-Sec3	0.0829 (0.0698)	4.7057 (3.186)	0.5765	0.5576	10.401 (3.474)	1.2743	0.6630
10BL-Sec5	0.0878 (0.0715)	5.3900 (3.401)	0.6337	0.5852	10.972 (3.563)	1.2900	0.6422
10BL-Sec8	0.0905 (0.0666)	5.0337 (3.034)	0.6140	0.5015	10.676 (3.433)	1.3021	0.6417
10BL-Sec10	0.0836 (0.0582)	4.4800 (2.488)	0.5883	0.3909	9.032 (3.097)	1.1861	0.6053
10BL-Sec13	0.0804 (0.0660)	4.9120 (2.746)	0.6044	0.4179	9.946 (3.376)	1.2238	0.6317
10BL-Sec15	0.0724 (0.0563)	6.1502 (4.008)	0.7021	0.7663	11.289 (3.952)	1.2888	0.7449
10BL-Sec18	0.0964 (0.0773)	4.6920 (2.743)	0.5697	0.4061	10.186 (3.288)	1.2369	0.5832
10BL-Sec20	0.0884 (0.0704)	5.1089 (3.149)	0.6035	0.5067	10.691 (3.694)	1.2629	0.6971
10BL-3-D	0.0708 (0.0657)	2.7824 (1.958)	0.3814	0.5455	9.0747 (2.339)	1.2440	0.7787
10BS-3-D	0.0690 (0.0397)	2.2653 (1.529)	0.3590	0.4448	8.2154 (1.854)	1.3019	0.6535
20BL-3-D	0.1132 (0.0959)	1.6633 (1.472)	0.2743	0.4465	7.8134 (1.897)	1.2888	0.7409

^a Abbreviations: (MAF, SDAF), mean and standard deviation of local area and volume fraction in μm^2 ; (MSND, SDSND), mean and standard deviation of (S-S) nearest-neighbor distance in μm ; (QS), Q-ratio for (S-S) nearest-neighbor distance; (RS), R-ratio for (S-S) nearest-neighbor distance; (MCND, SDCND), mean and standard deviation of (C-C) nearest-neighbor distance in μm ; (QC), Q-ratio for (C-C) nearest-neighbor distance, (RC), R-ratio for (C-C) nearest-neighbor distance.

start at around a value 2.5 μm , which correspond to the minimum distance between particle centres.

4.3.2. Local area and volume fractions

Local area or volume fraction, measured as a ratio of the particle size to that of the associated Voronoi cell created by tessellation, is a good indicator of local distribution. The statistical mean (MAF) and standard deviation (SDAF) of local area and volume fraction for various 2-D sections and the three 3-D microregions are tabulated in Table 2. The high values of standard deviation compared to the mean signals considerable variations in both area and volume fractions. The mean section area fractions are generally higher than the 3-D volume fractions, consistent with a simple analytical formula:

$$\frac{\text{Area fraction}}{\text{Volume fraction}} = \frac{3}{2} \left(\frac{a}{b} \right) \geq 1$$

for a uniform cubic representative volume element (RVE) of dimension a with a spherical particle of diameter b , sectioned at the middle. The effect of particle size on the local volume fraction is inferred by MAF for the 10BS composite being lower than that for the 10BL composite. The probability density function $f(A)$ of the local area and volume fractions are plotted in Fig. 7(a). All 2-D sections of the 10BL composite were found to have very similar variations and values and hence only the mean is plotted. The peaks in $f(A)$ for 3-D are considerably higher than those for 2-D sections and occur for nearly the same values of volume fraction. The peaks are consequences of steep gradients due to large concentrations in the local volume fraction. Smaller volume fractions are more probable than the larger ones as seen by the rather early peaks. For the 10BL composite, the higher concentration at low

volume fractions confirms that particles are closer in 3-D, than they appear in 2-D micrographs. The peaks are found to be highest at low values of volume fraction for the 10BL composite signalling a preponderance of relatively sparse regions.

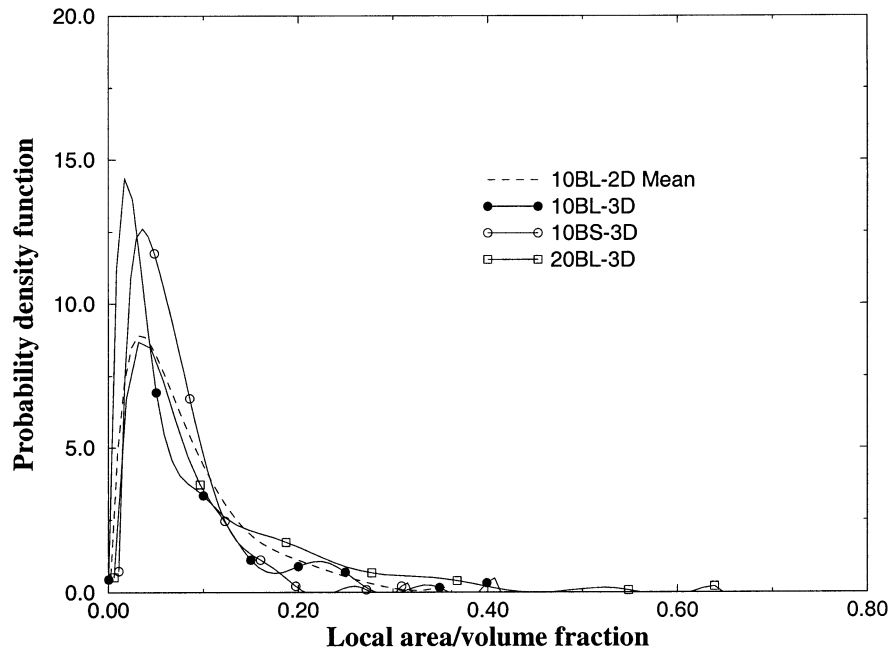
4.3.3. Neighbor distances

Near and nearest-neighbor distances are indicators of interactions in spatial processes and may be computed as the distance between particles that share a common edge of an associated Voronoi cell. Two distances, viz. the surface to surface (S-S) and center to center (C-C) distances are considered. The S-S neighbor distance is obtained by minimizing the surface distance between two ellipsoids, while the C-C is determined from centroidal coordinates. In general, the S-S distance is a better indicator since it reflects the effects of both size and shape on the distributions. Various statistics for the nearest neighbor and mean neighbor distances are tabulated in Table 2. Two ratios have been utilized in [20] for delineating spatial patterns in low volume fraction heterogeneous fields. They are:

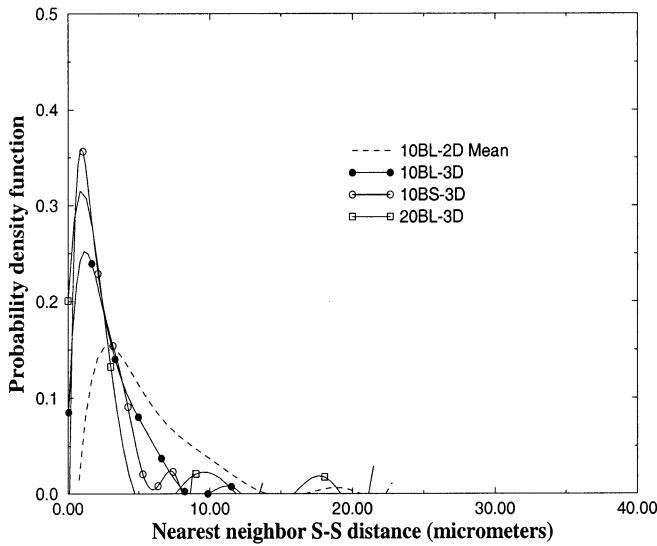
$$Q = \frac{E_{ob}(\bar{r})}{E_{pp}(\bar{r})} \quad \text{and} \quad R = \frac{E_{ob}(s^2)}{E_{pp}(s^2)}$$

where $E_{ob}(\bar{r})$ is the observed mean of near neighbor distance, $E_{pp}(\bar{r})$ is the expected mean of near neighbor distance for a Poisson process, $E_{ob}(s^2)$ is the observed variance of near neighbor distance, and $E_{pp}(s^2)$ is the expected variance of near neighbor distance for a Poisson process. The expressions for the expected means and variances for a 2- and 3-D Poisson distribution are given in [20,22,55] as:

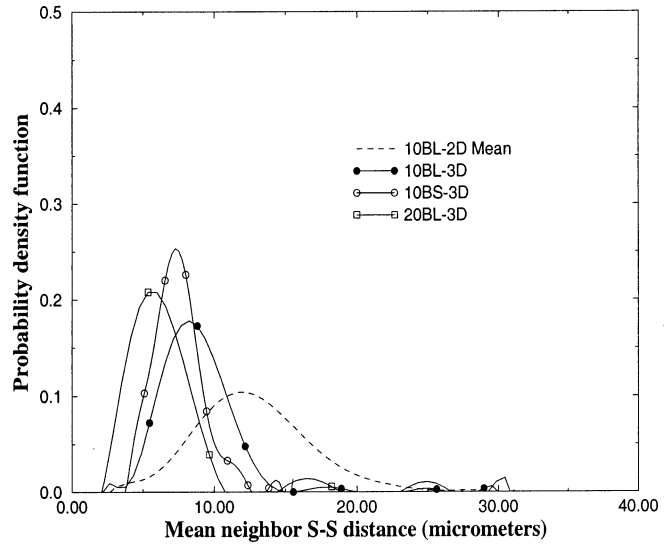
$$E_{pp}(\bar{r}) = 0.5 \left(\frac{N}{A} \right)^{-\frac{1}{2}}, \quad E_{pp}(s^2) = \frac{4 - \pi}{4\pi} \left(\frac{N}{A} \right)^{-1} \quad \text{in 2D}$$



(a)



(b)



(c)

Fig. 7. (a) Probability density function of local area/volume fraction; (b) probability density function of S–S nearest-neighbor distance; and (c) probability density function of mean near-neighbor distances.

$$E_{pp}(\bar{r}) = 0.89297951 \left(\frac{4}{3} \pi \frac{N}{V} \right)^{-\frac{1}{3}},$$

$$E_{pp}(s^2) = 0.1053328847 \left(\frac{3}{4} \pi \frac{N}{V} \right)^{-\frac{2}{3}} \quad \text{in 3D} \quad (11)$$

where N/A and N/V are the area and volume density of points, respectively. The mean S–S and C–C nearest-neighbor distances in Table 2 are lower for 3-D mi-

crostructures than for the 2-D sections. This illustrates again that 3-D particles are actually nearer than observed in 2-D sections. The mean distance between the larger particles in low volume fraction 10BL composite is the largest, while that for the high volume fraction 20BL composite is the smallest. For relatively small volume fractions (approximately 5%) with small particles, deviations of Q -ratio and R -ratio from unity are

known to distinguish hard-core patterns from clusters as shown in [20]. In general, the following classifications are provided in [20]:

- $Q \approx 1, R \approx 1$ for random point sets;
- $Q > 1, R < 1$ for short-range ordered sets;
- $Q < 1, R < 1$ for clustered sets;
- $Q < 1, R > 1$ for clusters in a background of Poisson distribution.

From Table 2, the ratios for the S–S distances are found to be $Q < 1, R < 1$ which point to clustering, while those for C–C distances are found to be $Q > 1, R < 1$ denoting clusters in random background. However the above criteria cannot be interpreted with confidence for these microstructures, since the particle sizes are large and the volume fractions are high.

The probability density functions of the S–S nearest-neighbor distances ($f(d_{NN})$) and S–S mean near-neighbor distances ($f(d_{MN})$) are plotted in Fig. 7(b) and (c), respectively. While peaks in $f(d_{NN})$ for nearest neighbor are of different intensity, they occur at nearly the same range of nearest-neighbor distances for all three materials and also for the 2-D sections. This is interesting since it reveals that the nearest distances are similar for all materials. The peaks are higher for 10BS and 20BL materials than for the 10BL material implying larger number of neighbors at nearly similar distances for the former materials. The observations are quite different for the $f(d_{MN})$ plots of mean neighbor distances. The peaks are considerably lower and do not occur at similar near-neighbor distances for different materials, especially for the 2-D sections. This is a consequence of averaging between neighbors. The zero values in $f(d_{NN})$ and $f(d_{MN})$ correspond to relatively large distances for which a near neighbor does not exist. The absence of multiple peaks in $f(d_{NN})$ indicate the lack of clustering. The prolonged tails for the 2-D sections are due to larger inter-particle distances in the projected sections. In Fig. 8(a), the cumulative distribution function $f(d_{RN})$ is plotted. This is the probability of the normalized ratio RN of S–S nearest-neighbor distance to equivalent size EQS and has been used as a distinguishing parameter for patterns in [6]. The characteristics of $f(d_{RN})$ plots are found to be very similar to the $f(d_{NN})$ plots in this study. The minimum nearest-neighbor distances are plotted as a function of the mean near-neighbor distances in Fig. 8(b). In this plot, data from several 2-D sections are seen to be clustered. A clear separation is seen between 2- and 3-D, and also between the different materials. Considerably smaller distances are noted for the 3-D microstructures. There is a large dispersion in the near-neighbor distances as seen from comparison of mean and minimum values.

4.4. Morphological Anisotropy

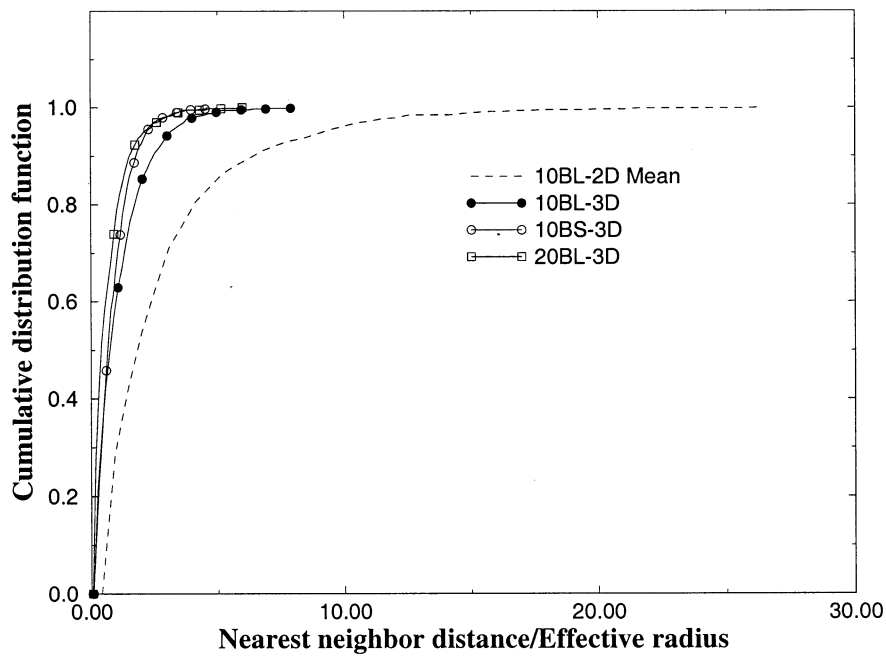
Local alignment or directionality in microstructural morphology is known to have a strong effect on the anisotropy of material behavior. Such directionalities may include (a) directionality in spatial distributions and (b) preferred orientation of the particles. A few measures are evaluated in this section for detecting geometric directionality.

4.4.1. Nearest neighbor orientation

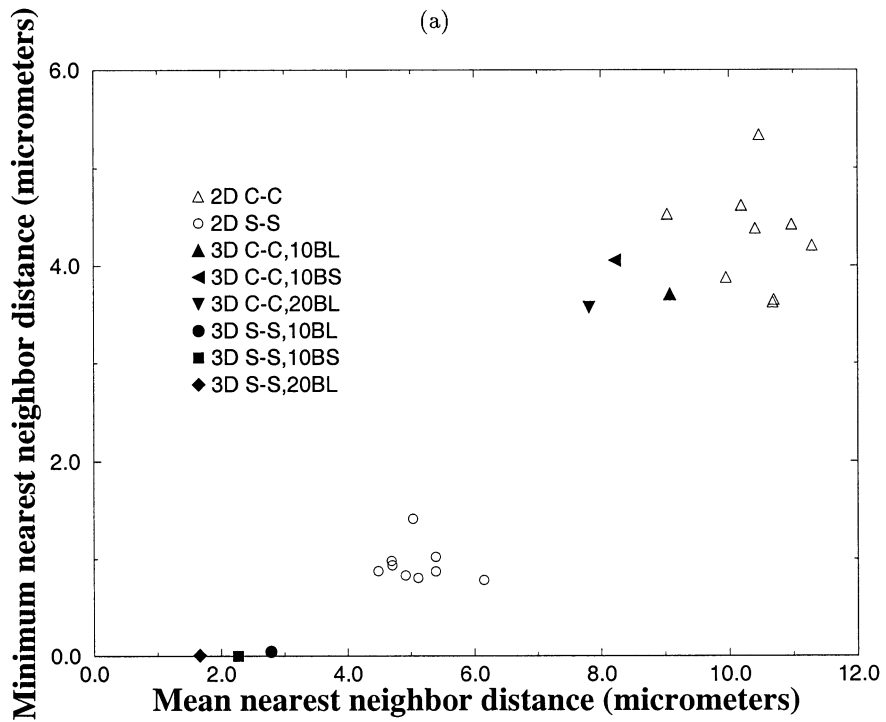
The nearest neighbor orientation is defined as the included angle between a line joining centroids of a particle and its nearest neighbor, and a designated baseline. All angles are equally likely for random distributions, but certain angles are expected to dominate for aligned or banded dispersions. The percentage of nearest neighbors are plotted as a function of orientation in Fig. 9(a). Results are analyzed for two 2-D sections and 3-D microstructure of the 10BL composite. For 2-D, the baseline is chosen to be the x -axis (extrusion direction), while for 3-D this may be the x -, y - or z -axes. Lack of a strong preferred orientation is indicated by relatively small peaks in these plots. The variation profile in nearest neighbor orientations for the 2-D sections is considerably different from those for 3-D. For 3-D the maximum percentage is near the 90° angle with all three baseline directions. However there are multiple peaks of preferred orientations for the 2-D sections.

4.4.2. Mean intercept cell length

The mean intercept length of the Voronoi cells in different directions is used as another tool to quantify anisotropy in spatial distribution. The intercept length in a given direction is measured as the length of a straight line within a Voronoi cell, that passes through the particle centroid in that direction. To evaluate mean intercept lengths, radial lines are drawn at regular angular intervals. For 2-D sections, the angles are between 0 and 360° . For 3-D, the angular orientations are expressed in terms of ϕ and θ as shown in Fig. 9(c). For each angle ϕ with the z -axis, the mean intercept length is calculated at equal intervals of angle θ in the range 0 – 360° . Intercepts for each cell along every radial line are then recorded and averaged over all Voronoi cells in the microstructure. In Fig. 9(b) the mean intercept length for 2-D sections of the composites are plotted as a function of the radial angle. The lack of strong spikes implies weak anisotropy in these sections. A mild orientation preference is observed near 0 , 180 and 360° directions which correspond to the extrusion direction. It is interesting to note that the plots for all three material sections match closely, especially for the 10BS and 20BL materials. The mean intercept length is higher for the 10BL material due to sparsity in the



(a)



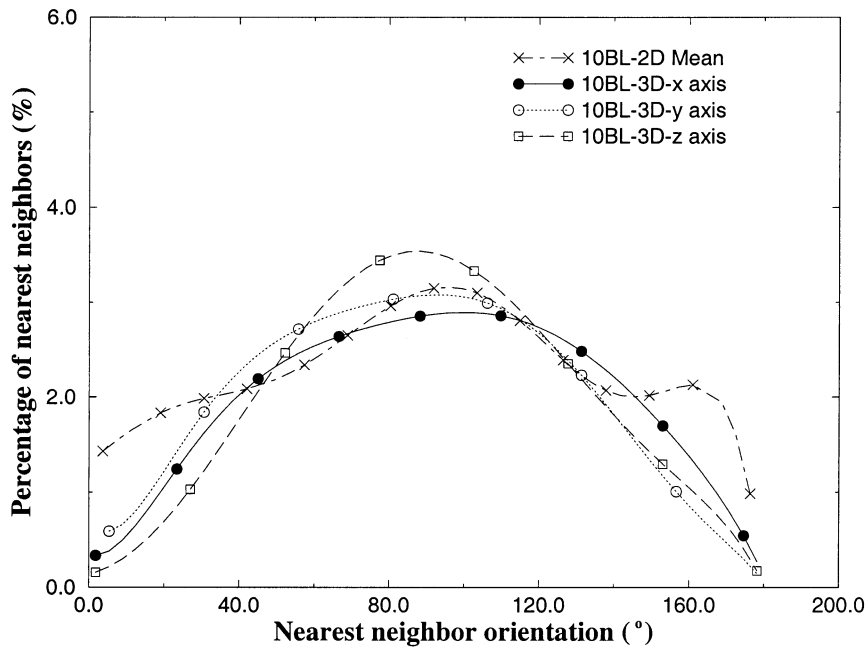
(b)

Fig. 8. (a) Cumulative distribution function for the ratio of nearest-neighbor distance to effective particle radius. (b) Plot of minimum to mean nearest-neighbor distance.

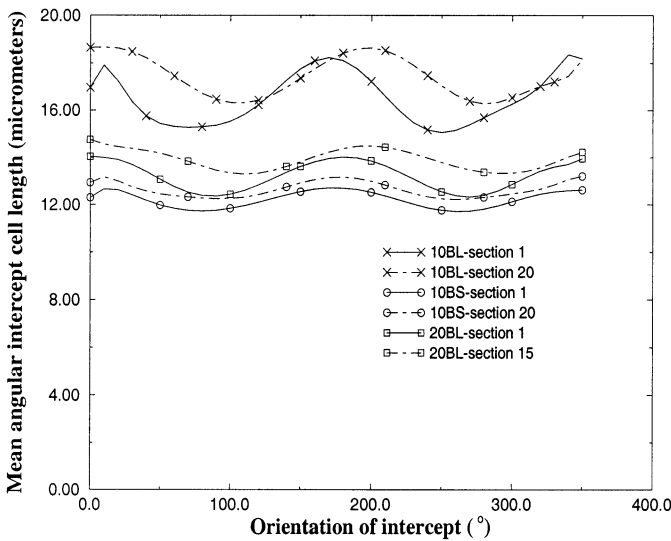
particle distribution. Fig. 9(c) is a plot of the mean intercept length for the 3-D 10BL material. The plots for various angles ϕ show almost no preferred orientation and therefore the microstructure is expected to exhibit isotropy.

4.4.3. Measures of particle orientation

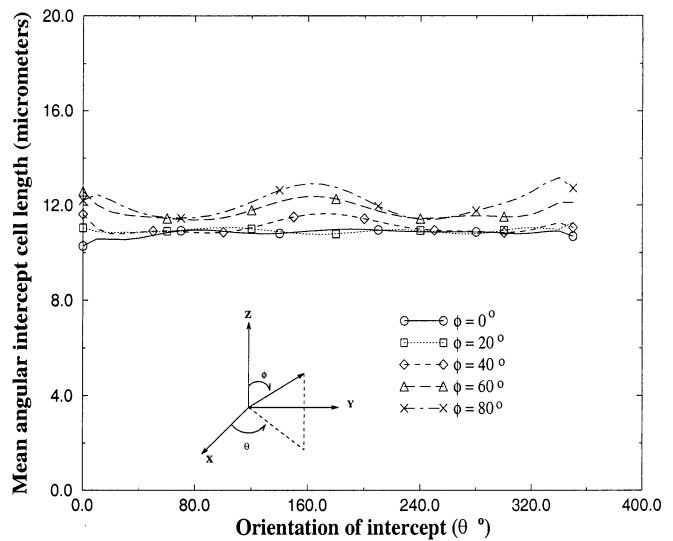
Two measures are introduced to detect preferred directionality in particle orientation. They are labeled as (a) mean major axis length in a given direction and (b) major axis orientation. The mean length in a given



(a)



(b)

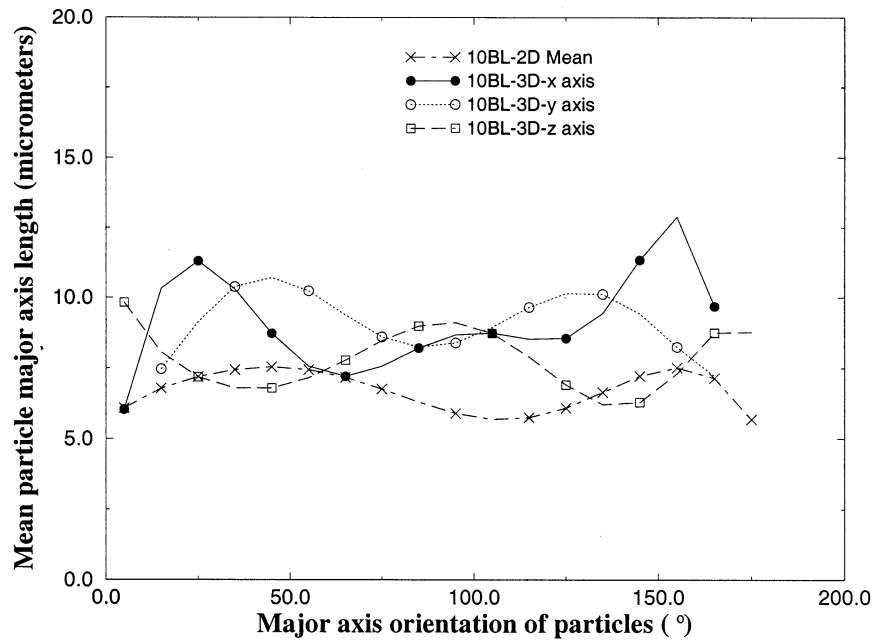


(c)

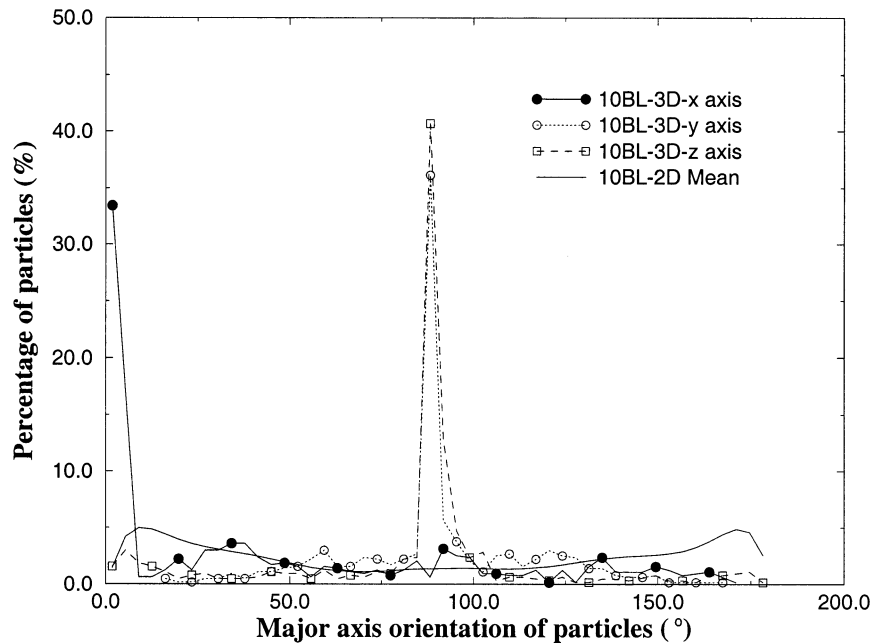
Fig. 9. Anisotropy characterization: (a) percentage of nearest neighbors as a function of orientation; (b) 2-D mean angular intercept cell lengths as a function of orientation for 10BL, 10BS and 20BL composite; (c) 3-D mean angular intercept cell lengths as a function of orientation for 10BL composite.

direction is calculated as the total of major axis lengths of all particles oriented in this direction, divided by the corresponding number of particles. The mean major axis lengths as a function of orientation are plotted in Fig. 10a for the mean 2-D section and 3-D microstructure of the 10BL composite. The orientations in 3-D are measured with respect to the x -, y - and z - axes. The mean major axis lengths do not change significantly

with orientation and do not show a strong bias. Fig. 10(b) is a plot of the percentage of particles with similar major axis orientations. Here the peaks are clearly for 0° with the x -axis and 90° with the y and z axes, which correspond to the extrusion direction. The mean 2-D plot does not show any defined peak. The latter plot is thus a better discriminator for particle directionality. The results show that even though the spatial distribu-



(a)



(b)

Fig. 10. Anisotropy characterization: (a) mean particle major axis length as a function of orientation for 10BL composite; (b) percentage of particles as a function of major axis orientation for 10BL composite.

tions may not have any strong directionality, particles themselves may have a preferred orientation due to pre-straining.

5. Conclusions

This sequence of papers perhaps for the first time provides 3-D physical characterization of the phase and

damage structure for particle reinforced aluminum matrix composite materials. The serial sectioning method enables construction of detailed 3-D microstructures at fairly high resolution from a series of parallel 2-D section micrographs. While this process is tedious, it is perhaps the best current method for 3-D visualization, microstructure reconstruction and image analysis at a high resolution (3–5 μm) of particle size and spacing. This paper presents a systematic approach to 2- and

3-D microstructural characterization by a combination of serial sectioning and computational methods. Three different types of materials characterized by different volume fractions and particle sizes are analyzed. Through a comparative study of microstructural properties of 3-D and corresponding 2-D sections, differences in characteristics are investigated and the need for 3-D models established.

The 3-D microstructural image of each specimen is created by stacking approximately 15–20 parallel sections at an average distance of 1.5–2.75 μm each. In addition, equivalent microstructures with elliptical (in 2-D) and ellipsoidal (in 3-D) particles are computationally simulated. This process involves equating the zero, first and second moments of the exact microstructures with known expressions of moments for the ellipsoids or ellipses in terms of the principal axes lengths. The equivalent microstructures retain the major statistical properties and distributions of the actual microstructures and are computationally very efficient. The microstructures are then tessellated into 2- and 3-D Voronoi cells which represent the basic structural elements. Tessellation has important advantages in image analysis and modeling. It facilitates generation of geometric parameters like local area or volume fraction, nearest-neighbor distance, radial distribution functions and functions of preferred directionalities.

In the image analysis process, statistical functions like mean and standard deviations, cumulative distribution and probability density functions, and second order intensity and pair distribution functions of various morphological parameters are evaluated both qualitatively and quantitatively. The microstructural characterization is divided into three categories, viz. (a) particle geometry, (b) spatial distribution and (c) preferred orientation. Distribution functions of size, aspect ratio and form factors reveal that while particle sizes and shapes vary considerably, a few sizes and shapes are clearly dominant. The spatial distribution functions of radial location, local volume fractions and near-neighbor distances reveal almost no clustering in the materials considered. This is expected for the fabrication process. In the analysis for identifying anisotropy, particles are found to have preferred orientations especially along the extrusion direction. However the spatial distributions of particles are quite random with nearly isotropic behavior.

The difference in morphological characteristics and statistics of 3- and 2-D sections is an important outcome of this study. With almost all the criteria considered, the characterization functions for 2-D sections are significantly different from those for 3-D microstructures, although they are generally quite consistent within the different 2-D sections. In 3-D, the particles are located much closer together than is apparent from their projected 2-D sections. Considerable difference is also seen in the orientation distributions.

Stereological methods predict 3-D distributions by statistical extrapolation of known 2-D information. Two such methods are utilized in this study for quantitatively evaluating the ability of these methods to predict important microstructural features like sizes, local volume fractions, near-neighbor spacings etc. These define the microstructural ‘triggers’ that control damage evolution and dominant shear band and crack nucleation. The studies reveal that while they have some potential for size predictions, their capability for predicting shapes, orientations and near neighbor spacings may be limited. It is clear that a full 3-D characterization is required for a comprehensive understanding of the damage evolution process. This is the subject of the second part of this sequence of papers.

Acknowledgements

The authors would like to thank Warren H. Hunt for offering the materials. The help of Byrl J. Johnson, Sally A. Jankosky, Rich Tallarico, D.H. Ringer, John C. Vilsack and W.R. Vogt of ALCOA Technical Center for help on image analysis, serial sectioning, specimen preparation and hardness measurement is highly appreciated. The first two authors have been supported by the United States Army Research Office through grant No. DAAH04-95-1-0176 (Program Director: Dr K.R. Iyer), by the National Science Foundation through a NSF Young Investigator grant (Grant No. CMS-9457603), by the Air Force Office of Scientific Research through grant No. F49620-98-1-01-93 (Program Director: Dr O.O. Ochoa), and by a grant from the ALCOA Technical Center. This sponsorship is gratefully acknowledged.

References

- [1] J.R. Brockenbrough, S. Suresh, H.A. Wienecke, *Acta Metall. Mater.* 39 (1991) 735.
- [2] T. Christman, A. Needleman, S. Suresh, *Acta Metall. Mater.* 37 (1989) 3029.
- [3] C.W. Nan, D.R. Clarke, *Acta Mater.* 44 (1996) 3801.
- [4] S. Moorthy, S. Ghosh, *Comp. Meth. Appl. Mech. Eng.* 151 (1998) 377.
- [5] S. Ghosh, S. Moorthy, *Acta Metall. Mater.* 46 (1998) 965.
- [6] W.H. Hunt, *Microstructural Damage Processes in an Aluminum Matrix-Silicon Particle Composite Model System*, Ph.D Thesis, Carnegie Mellon University, Pittsburgh, USA, 1992.
- [7] M.T. Kiser, F.W. Zok, J.R. Brockenbrough, W.H. Hunt, D.S. Wilkinson, in: J.J. Lewandowski W.H. Hunt (Eds.), *Intrinsic and Extrinsic Fracture Mechanisms in Inorganic Composite Systems*, The Minerals, Metals and Materials Society, 1995, pp. 25.
- [8] J.J. Lewandowski, C. Liu, W.H. Hunt, *Mater. Sci. Eng. A* 107 (1989) 241.
- [9] C. Liu, S. Pape, J.J. Lewandowski, in: H. Ishida (ed.), *Proceedings of the ICCI-II*, Elsevier, New York, 1988, pp. 513.

- [10] J.J. Lewandowski, C. Liu, in: D. Wilkinson (Ed.), Proceedings of the Metals Society of the Canadian Institute of Mining and Metallurgy, vol. 2, Pergamon Press, 1988, pp. 23.
- [11] J.J. Lewandowski, C. Liu, W.H. Hunt, Jr., in: P. Kumar, K.M. Vedula, A.M. Ritter (Eds.), Powder Metallurgy Composites, TMS-AIME, Warrendale, PA, 1987, pp. 117.
- [12] P.M. Singh, J.J. Lewandowski, Metall. Trans. A 24A (1993) 2531.
- [13] P.M. Singh, J.J. Lewandowski, Metall. Trans. A 26A (1995) 2911.
- [14] P.M. Singh, J.J. Lewandowski, Scripta Metall. 29 (1993) 199.
- [15] P.M. Singh, J.J. Lewandowski, in: J.J. Lewandowski, W.H. Hunt (Eds.), Intrinsic and Extrinsic Fracture Mechanisms in Inorganic Composite Systems, The Minerals, Metals and Materials Society, 1995, pp. 57.
- [16] A. Vaidya, J.J. Lewandowski, in: J.J. Lewandowski, W.H. Hunt (Eds.), Intrinsic and Extrinsic Fracture Mechanisms in Inorganic Composite Systems, The Minerals, Metals and Materials Society, 1995, pp. 147.
- [17] J. Llorca, M. Elices, in: J.J. Lewandowski, W.H. Hunt (Eds.), Intrinsic and Extrinsic Fracture Mechanisms in Inorganic Composite Systems, The Minerals, Metals and Materials Society, 1995, pp. 15.
- [18] P.M. Mummery, B. Derby, C.B. Scruby, Acta Metall. Mater. 41 (1993) 1431.
- [19] Y. Brechet, J.D. Embury, S. Tao, L. Luo, Acta Metall. Mater. 39 (1993) 1781.
- [20] W.A. Spitzig, J.F. Kelly, O. Richmond, Metallography 18 (1985) 235.
- [21] P.J. Wray, O. Richmond, H.L. Morrison, Metallography 16 (1983) 39.
- [22] R.K. Everett, J.H. Chu, J. Comp. Mater. 27 (1992) 1128.
- [23] R. Pyrz, Comp. Sci. Tech. 50 (1994) 197.
- [24] R. Pyrz, Mater. Sci. Eng. A 177 (1994) 253.
- [25] R. Pyrz, in: P. Pedersen (Ed.), Optimal Design with Advanced Materials, Elsevier, Amsterdam/New York, 1993, pp. 81.
- [26] Y. Xi, Mater. Charact. 36 (1996) 11.
- [27] S. Ghosh, Z. Nowak, K. Lee, Acta Mater. 45 (1997) 2215.
- [28] S. Ghosh, Z. Nowak, K. Lee, Comp. Sci. Tech. 57 (1997) 1187.
- [29] D.J. Lloyd, Acta Metall. Mater. 39 (1991) 59.
- [30] J.D. Embury, F. Zok, D.J. Lahaie, W. Poole, in: J.J. Lewandowski, W.H. Hunt (Eds.), Intrinsic and Extrinsic Fracture Mechanisms in Inorganic Composite Systems, The Minerals, Metals and Materials Society, 1995, pp. 1.
- [31] F. Zok, unpublished data.
- [32] M. Li, S. Ghosh, T.N. Rouns, H. Weiland, O. Richmond, W. Hunt, Mater. Charact. 41 (1998) 81.
- [33] E.R. Weibel, Stereological Methods: Theoretical Foundation, vol. 2, Academic Press, London, 1980.
- [34] J.J. Norden, in: Chermant, J.-L. (Ed.), Proceedings of the 7th International Congress for Stereology, Int. Soc. Ster., Caen, France, 1987, pp. 117.
- [35] J.C. Russ, Practical Stereology, Plenum Press, New York, 1986.
- [36] E.B. Jensen, H.J.G. Gundersen, in: Proceedings of the 7th International Congress for Stereology, Caen, France, 1987, pp. 25.
- [37] S.A. Saltykov, Stereometric Metallograph, 2nd ed., State Publishing House for Metals and Sciences, Moscow, 1958.
- [38] S.A. Saltykov, Stereology, in: Elias, H. (Ed.), Proceedings of the 2nd International Conference for Stereology, Springer-Verlag, New York, 1967, pp. 163.
- [39] R.T. DeHoff, Trans. AIME 224 (1962) 474.
- [40] L.M. Cruz-Orive, J. Microsc. 112 (1978) 153.
- [41] T.N. Rouns, J.M. Fridy, K.B. Lippert, O. Richmond, in: M.P. Anderson, A.D. Rollet (Eds.), Simulation and Theory of Evolving Microstructures, The Minerals and Materials Society, Warrendale, PA, 1990, pp. 269.
- [42] J.M. Fridy, K. Marthinsen, T.N. Rouns, K.B. Lippert, E. Nes, O. Richmond, Proceedings of the 3rd International Conference on Aluminium Alloys, Trondheim, Norway, vol. 2, 1992, pp. 333.
- [43] J.R. Brockenbrough, J.M. Fridy, J.L. Teply, in: D.O. Thompson, D.E. Chimenti (Eds.), Quantitative Nondestructive Evaluation, vol. 13, Plenum Press, New York/London, 1994, pp. 21.
- [44] S.K. Burke, S.McK. Cousland, C.M. Scala, Mater. Forum 18 (1994) 85.
- [45] R.G. King, P.M. Delaney, Mater. Forum 18 (1994) 21.
- [46] M. Berman, L.M. Bischof, E.J. Breen, G.M. Peden, Mater. Forum 18 (1994) 1.
- [47] J.Y. Buffiere, E. Maire, C. Verdu, et al., Mater. Sci. Eng. A 234–236 (1997) 633.
- [48] R.N. Yancey, G.Y. Baakli, in: Proceedings of the ASME International Gas Turbine and Aeroengines Congress, Cincinnati, Ohio, USA, May 24–27, 1993.
- [49] H. Weiland, T.N. Rouns, J. Liu, Z. Metallkd 85 (1994) 592.
- [50] J.J. Lewandowski, M. Manoharan, W.H. Hunt, Mater. Sci. Eng. A 172 (1993) 63.
- [51] SPYGLASS Slicer, Quick Tour and Reference, Version 1.0, Spyglass, Champaign, IL 61826, 1994.
- [52] SPYGLASS Transform, Quick Tour and Reference, Version 3.0, Spyglass, Champaign, IL 61826, 1994.
- [53] S. Ghosh, S.N. Mukhopadhyay, Comput. Struct. 41 (1991) 245.
- [54] N. Raghavan, P. Goel, S. Ghosh, J. Comput. Graph. Stat. (submitted for publication).
- [55] H. Schwarz, H.E. Exner, J. Microsc. 129 (1983) 155.